Remote Sens. **2011**, *3*, 1492-1515; doi:10.3390/rs3071492

OPEN ACCESS

Remote Sensing

ISSN 2072-4292

www.mdpi.com/journal/remotesensing

Article

Sensitivity of Depth-Integrated Satellite Lidar to Subaqueous Scattering

Jonathan S. Barton [1] and Michael F. Jasinski [2,*]

[1] Universities Space Research Association, Goddard Earth Sciences Technology and Research (GESTAR), Goddard Space Flight Center, Code 614.1, Greenbelt, MD 20771, USA; E-Mail: jonathan.barton@nasa.gov

[2] Hydrological Sciences Branch, NASA Goddard Space Flight Center, Code 614.3, Greenbelt, MD 20771, USA

* Author to whom correspondence should be addressed; E-Mail: michael.f.jasinski@nasa.gov; Tel.: +1-301-614-5782; Fax: +1-301-614-5808.

Received: 13 May 2011; in revised form: 26 June 2011 / Accepted: 29 June 2011 / Published: 11 July 2011

Abstract: A method is presented for estimating subaqueous integrated backscatter using near-nadir viewing satellite lidar. The algorithm takes into account specular reflection of laser light, laser scattering by wind-generated foam as well as sun glint and solar scattering from foam. The formulation is insensitive to the estimate of wind speed but sensitive to the estimate of transmittance used in the atmospheric correction. As a case study, CALIOP data over Tampa Bay were compared to MODIS 645 nm remote sensing reflectance, which previously has been shown to be nearly linearly related to turbidity. The results indicate good correlation on nearly all CALIOP cloud-free dates during the period 2006 through 2007, particularly those with relatively high atmospheric transmittance. The correlation decreases when data are composited over all dates but is still statistically significant, a possible indication of variability in the biogeochemical composition in the water. Overall, the favorable results show promise for the application of satellite lidar integrated backscatter in providing information about subsurface backscatter properties, which can be extracted using appropriate models.

Keywords: lidar; CALIOP; CALIPSO; backscattering; turbidity; water quality; Tampa Bay

1. Introduction

The US Environmental Protection Agency [1] ranked siltation and its attendant turbidity as one of the most widespread pollutants in the United States. It affects rivers, lakes, reservoirs, and coastal waters, adversely affecting aquatic habitat, drinking water treatment facilities, recreational use, and commercial navigation and fisheries. High levels of sediment in the water column reduce spawning grounds and reduce the availability of food supplies for aquatic life. High concentrations of sediment may lead to rapid deposition, causing changes in coastal or fluvial morphology, which may lead to navigational hazards or increase flood risks for the region. Regions of low turbidity due to low suspended sediment concentrations) may experience rapid erosion leading to entrenchment and bank failure in a fluvial system or to beach erosion and barrier island collapse in the coastal environment.

Remote sensing of turbidity has a long history in the scientific literature. Descriptions of qualitative analyses relating Landsat Multispectral Scanner System (MSS) surface radiance to turbidity and suspended sediment concentration appear in the literature as early as 1973 (e.g., [2-4]). Quantitative algorithms began to appear in the 1970s, and ranged in complexity from linear relationships between MSS Band 5 radiance and suspended sediment concentration to polynomial fits to the ratio of MSS radiances in different bands (see [5] and references therein). More rigorous, model-driven algorithms were in development by the late 1970s (e.g., [5]) with the incorporation of diffuse reflection models developed earlier in the decade (e.g., [6-8]). Curran and Novo [9] summarized early efforts, though several significant studies post-date this work (e.g., [10-14]). More recently, good results have been obtained in retrieving turbidity using off-nadir Moderate Resolution Imaging Spectroradiometer (MODIS) imagery (e.g., [15]). They indicate a near linear relation between *in situ* turbidity and red reflectance when applied to individual regions. However, formulation of a global algorithm applicable to all regions has not yet been demonstrated.

Spaceborne lidars have been used in earth observation since the mid-1990s when BALKAN flew on the space station MIR [16]. A large fraction of these lidars have fallen on water. Unlike their airborne counterparts, spaceborne lidars have not possessed the vertical resolution necessary to profile the water column. This paper offers to add value to existing lidar datasets by using the depth-integrated lidar backscatter to extract information about turbidity or scattering within the water column.

The use of a 532 nm laser to study water turbidity was pioneered in the 1980s with theoretical work by Gordon [17], and by Phillips *et al.* [18]. Experiments into the use of a ship-mounted laser (532 nm) for measuring the optical properties of seawater were carried out by Ivanov *et al.* [19] in the Soviet Union. Empirical studies using the Australian Weapons Research Establishment Laser Airborne Depth Sounder (WRELADS) sensor by Phillips *et al.* [20], and by Billard [21] showed that estimates of both backscattering and effective attenuation were possible from depth sounding lidars. The 532 nm channel is of particular interest in both turbidity monitoring and in other hydrologic applications, because it lies close to the wavelength achieving maximum penetration into the water column [22].

Spaceborne lidars have been used very little for oceanography. Lancaster *et al.* [23] used the GLAS (Geoscience Laser Altimeter System) lidar on the ICESat (Ice, Cloud, and land Elevation Satellite) platform to detect water surface reflectance and compared that with the predicted theoretical reflectance from QuikSCAT (Quick Scatterometer) wind speeds. Hu *et al.* [24] used the CALIOP (Cloud-Aerosol Lidar with Orthogonal Polarization) lidar on the CALIPSO (Cloud-Aerosol Lidar and

Infrared Pathfinder Satellite Observations) satellite to measure wind speed, and compared the results to AMSR-E (Advanced Microwave Scanning Radiometer-EOS) wind speed measurements. They used the depolarization ratio available from CALIOP to remove the sea foam effect from the surface measurement.

The study detailed in this paper also uses the CALIOP lidar, which has a 30 m vertical resolution near the surface. CALIOP has a 90 m horizontal resolution, with centers spaced 333 m along track. CALIPSO flies in NASA's A-Train constellation, following Aqua by 73 ± 43 seconds. [25] As an active sensor, it is capable of making night-time measurements, and the ability to separate atmospheric returns from surface returns makes local atmospheric correction possible.

The overall approach is to estimate subaqueous backscatter as the residual term within an expression of total depth-integrated attenuated backscatter. Specifically, total, depth-integrated attenuated backscatter is formulated as the sum of all surface and subsurface effects. With total backscatter obtained from CALIOP, and other surface components modeled, the subsurface backscatter can be retrieved. Sensitivity analysis on the accuracy of the CALIOP data and on individual model components is used to delineate the limits and potential accuracy of the subsurface backscatter retrieval. Theoretical sensitivity analysis is followed by a test case over the Tampa Bay region of Florida.

2. Model Basis

The depth-integrated attenuated backscatter (at a wavelength of λ, in nm) received by a satellite from the surface bins can be represented as an attenuated sum of scattering returning from components of the target:

$$\gamma_\lambda = T_\lambda\left(\gamma_\lambda^w + \gamma_\lambda^f + \gamma_\lambda^s + \gamma_\lambda^{sf} + \gamma_\lambda^u\right) \quad (1)$$

where T_λ is the atmospheric transmittance (including aerosol effects, and along the lidar look direction), the variables γ_λ^w, γ_λ^f, γ_λ^s, γ_λ^{sf}, and γ_λ^u represent, respectively, the integrated backscatter due to specular reflection of the laser from the water surface, laser light scattered by foam on the water surface, the specular reflection of sunlight from the water surface, sunlight scattered by foam on the water surface, and particles in the underwater environment. The magnitudes of γ_λ^w, γ_λ^f, γ_λ^s, and γ_λ^{sf} are all primarily controlled by the wind and wave field. γ_λ^u is controlled by the number and properties of particulates present in the water column. Other possible components beyond the scope of this study and not listed in (1) include bottom scattering effects, scattering from surface slicks, and scattering by spray in regions of high winds. Details of each component are described below.

The goal of the modeling presented here is to allow the estimation of γ_{532}^u from satellite measurements of γ_{532}, and γ_{1064}, and the modeling of the other components. Surface wind speed and visibility estimates are used as inputs into the models.

2.1. Atmospheric Correction

A principal factor affecting the radiometric surface measurement is the atmospheric transmittance, which can be further subdivided into molecular, aerosol, and cloud transmittance. One advantage of using lidar technology compared with a passive sensor is the ability to separate the scattering due to

the atmospheric effects from the scattering at the surface based on the time of the photons' arrival at the satellite. The CALIPSO release products include an aerosol layer optical depth and a cloud layer optical depth product. These data, combined with temperature and pressure data from NASA's Global Modeling and Assimilation Office, and included in the CALIPSO release product, were used in the current work to develop a LOWTRAN 7 atmospheric model.

In the current study, optical depth of the cloud layers and aerosol layers were accounted for using the CALIOP data. However, optical depths of the clear air interstices, not available from the CALIOP archive, were evaluated using the LOWTRAN 7 model, resulting in a continuous profile of optical depth throughout the atmospheric column. The optical depths for the layers were summed (taking into account that the aerosol and cloud layers sometimes overlap), and a resulting total atmospheric optical depth and transmittance were obtained. To calculate the clear-air optical depths, default settings were used for the LOWTRAN 7 model, except for the input of relative humidity, temperature, pressure and ozone concentration data extracted from the Level 1 and Level 2 CALIOP products, and surface visibility was interpolated from historical airport records from around Tampa Bay. A sensitivity analysis showed that assuming a constant surface visibility of 23 km produced errors in the subaqueous integrated backscatter of less than 5%.

2.2. Specular Surface Reflection

Specular reflection from the water surface is by far the largest contribution to the total integrated attenuated backscatter. Specular reflection decreases as wave steepness increases and is extremely large in very calm waters. Hu *et al.* [24], citing Platt [26], Menzies *et al.* [27], and Tratt *et al.* [28], modeled the specular surface reflection as:

$$\gamma_{\lambda}^{w} = \frac{\rho_{\lambda}}{4\,\pi\,\sigma^{2} cos^{4}\theta}\, exp\left[\frac{-tan^{2}\theta}{2\sigma^{2}}\right] \tag{2}$$

where ρ_{λ} is the Fresnel specular reflection coefficient ($\rho_{532} \approx 0.0209$, $\rho_{1064} \approx 0.0199$), σ^{2} is the wave slope variance, and θ is the zenith angle of the sensor. In the present study, the small angle approximation is not made, as it was made by Hu *et al.*, because it can produce significant errors at low wind speed even for small angles such as the 0.3° pointing angle for CALIOP. Hu *et al.*'s composite model for the wave slope variance as a function of wind speed is employed:

$$\sigma^{2} = \begin{cases} U < 7 & 0.0146\sqrt{U} \\ 7 \le U < 13.3 & 0.003 + 0.00512\,U \\ U \ge 13.3 & 0.138 \log_{10} U - 0.084 \end{cases} \tag{3}$$

Although this model provides a reasonable guess at the backscattering when given a known wind speed, it is very sensitive to the wind speed. To overcome this sensitivity, one can exploit the fact that the only wavelength dependent term in (2) is ρ_{λ}, and also the fact that infrared light does not penetrate the ocean surface; *i.e.*, γ_{1064}^{u} is zero. The specular surface reflection in the green can then be formulated in terms of the total integrated attenuated backscatter in the infrared:

$$\gamma_{532}^{w} = \frac{\rho_{532}}{\rho_{1064}}\gamma_{1064}^{w} = \frac{\rho_{532}}{\rho_{1064}}\left(\frac{\gamma_{1064}}{T_{1064}} - \gamma_{1064}^{f} - \gamma_{1064}^{s} - \gamma_{1064}^{sf}\right) \tag{4}$$

where γ_{1064}^{f}, γ_{1064}^{s}, and γ_{1064}^{sf} are described in the subsequent sections. The resulting model is only weakly dependent on the accuracy of the wind speed estimate, especially for low wind speeds and for night measurements, when γ_{1064}^{s} and γ_{1064}^{sf} are zero.

An added benefit of this infrared-based approach is that deviations from the fully-developed sea models of Cox and Munk [29] or Bréon and Henriot [30] are accounted for implicitly, without the need for estimating fetch, wind direction, or bottom topography. This is particularly important in coastal zones, where sheltered waters can have very short fetches, and shallows can cause rapid and localized steepening of waves.

2.3. Lambertian Scattering from Foam

At relatively high wind speeds, the scattering of the lidar beam from whitecaps and foam streaks on the water surface can be a significant factor, particularly as the wave surface return becomes darker as the waves steepen. At wind speeds higher than about 10 m/s, the magnitude of foam scattering approaches that expected for subsurface scattering in low turbidity natural waters. As noted above, Hu *et al.* [24] used the depolarization ratio from the CALIOP lidar to model the foam contribution to the backscattering. However, depolarization may occur during scattering from foam or from hydrosols, so this type of model may eliminate the potential to retrieve information from the subsurface. The foam is therefore modeled as a Lambertian scattering process, from foam covering a fractional area, *W*, described by Callaghan and White [31]:

$$W = \begin{cases} U < 3.70 & 0 \\ 3.70 \le U < 10.1874 & 3.18 \times 10^{-5}(U - 3.70)^3 \\ U \ge 10.1874 & 4.82 \times 10^{-6}(U + 1.98)^3 \end{cases} \quad (5)$$

Moore *et al.* [32] modeled the reflectance of foam as a function of wind speed. In this model the reflectance of the foam is expressed as an "additional" reflectance, representing the increased reflectance of the ocean surface due to the foam. In the visible wavelengths, including 532 nm and at the upper limit of 670 nm, they expressed this additional reflectance as:

$$RSAR_{\le 670} = 3.14 \times 10^{-6} U^{2.55} \quad (6)$$

For the near infrared at 860 nm they expressed the additional reflectance, $RSAR_{860}$, as

$$RSAR_{860} = 0.22\ (1 - \exp[-4.2\ RSAR_{670}]) \quad (7)$$

The laboratory data of Frouin *et al.* [33] suggests an exponential decrease in the reflectance of foam with wavelength (λ, in nm) as shown in Figure 1:

$$RSAR_{\lambda > 670} = A[U] \exp\left[-k[U]\lambda\right] \quad (8)$$

At a given wind speed, the coefficient A and the decay constant k can be estimated by fitting to Equations (6) and (7). Repeating this process over a range of wind speeds, and using least squares polynomial regression, one can estimate A[U] and k[U] as follows.

$$A[U] = 1.53 \times 10^{-4} + U\left(-1.17 \times 10^{-4} + U\left(2.57 \times 10^{-5} + U(-2.27 \times 10^{-7} + U\ 1.74 \times 10^{-8})\right)\right) \quad (8a)$$

$$k[U] = 4.16 \times 10^{-4} + U\left(-3.02 \times 10^{-7} + U\left(9.86 \times 10^{-8} + U\left(5.30 \times 10^{-9} + U(-2.68 \times 10^{-11})\right)\right)\right) \quad (8b)$$

For wind speeds less than about 10 m/s, A[U] and k[U] can be approximated by their constant

first terms.

Figure 1. Data of Frouin *et al.* [33], which suggests an exponential function of wavelength. The correlation is not significant, with only four data points, but it suggests that exponential decay is a starting point upon which we can construct a model.

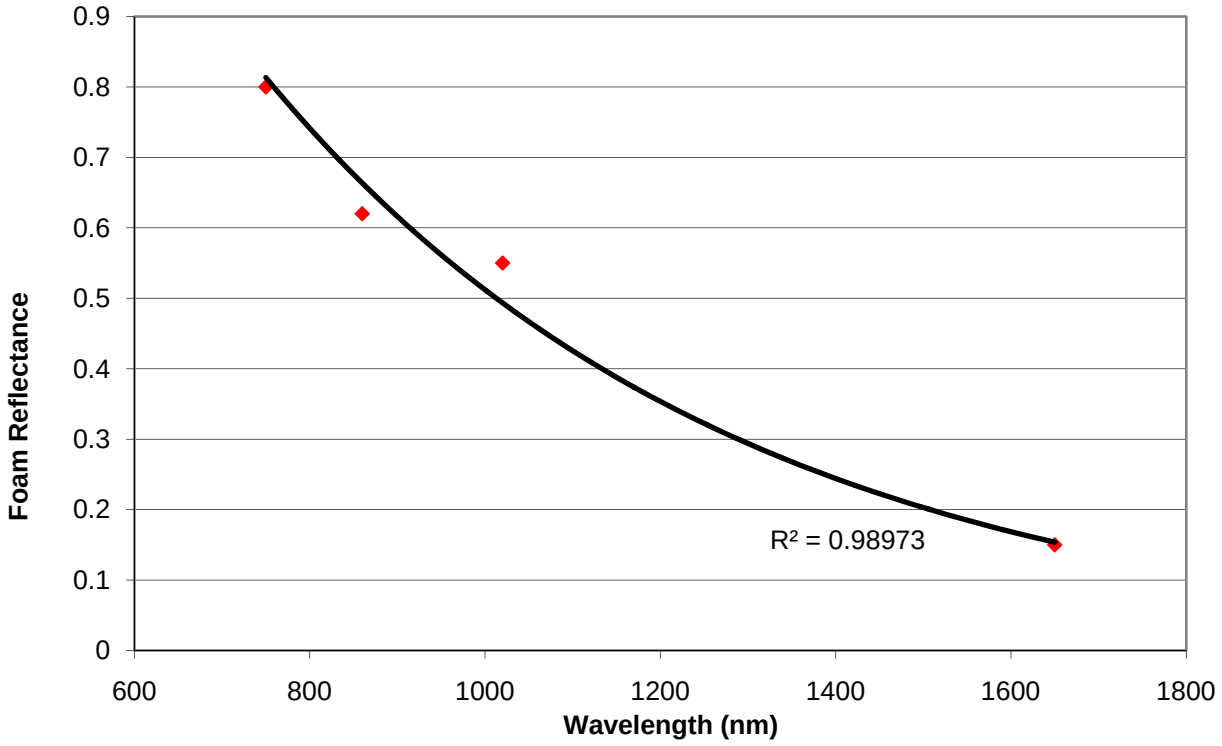

Using these results, and multiplying by $\cos\theta/\pi$ to convert between reflectance and Lambertian scattering, one can write the expression for the scattering due to the foam. Because the model presented above calculates the additional reflectance due to the foam, an estimate of the sea surface scattering without foam is also included or Equation (2). It is possible to use Equation 10(b) for the 532 nm lidar by replacing −1,064 k with −532 k in the exponential, and the same results will be obtained. Equation 10(a) can be used when efficiency is a concern. A graphical representation of these models is presented in Figure 2.

$$\gamma_{532}^{f} = W\left(\frac{\rho_{532}}{4\,\pi\,\sigma^2\cos^4\theta}\exp\left[\frac{-\tan^2\theta}{2\sigma^2}\right] + 3.14\times10^{-6}U^{2.55}\frac{\cos\theta}{\pi}\right) \quad (9a)$$

$$\gamma_{1064}^{f} = W\left(\frac{\rho_{1064}}{4\,\pi\,\sigma^2\cos^4\theta}\exp\left[\frac{-\tan^2\theta}{2\sigma^2}\right] + A[U]\exp\left[-1064k[U]\right]\frac{cos\,\theta}{\pi}\right) \quad (9b)$$

Figure 2. Model of backscatter due to Lambertian scattering from foam. Three wavelengths are shown. The black curve shows the model of Moore *et al.* [32] for visible wavelengths up to 670 nm (Equation (6)). This model is used for the 532 nm laser light. The blue curve is the model of Moore *et al.* [32] for 860 nm shortwave infrared (Equation (7)). The red curve shows an extrapolated model for 1,064 nm, created as described in the text as an exponential decay with wavelength perfectly fitting the two shorter-wavelength models. (Equation (8), where λ = 1,064 nm.)

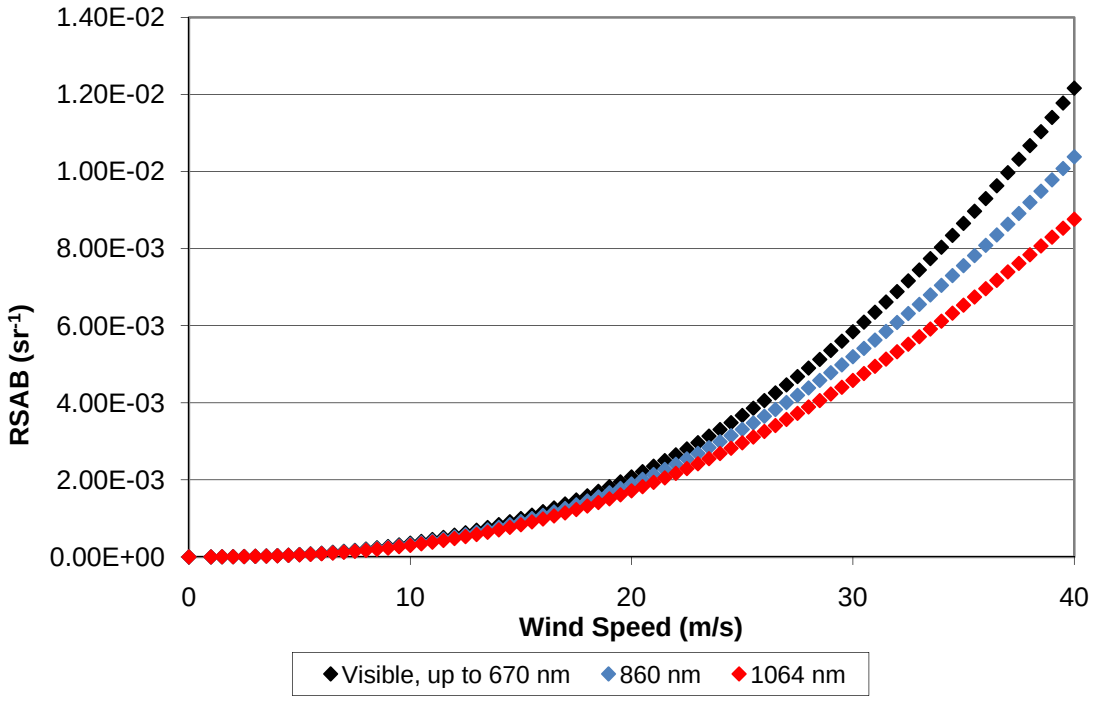

2.4. Sun Glint

At low solar zenith angles, and particularly for lidar sensors which may use low-power micropulse sensing, the presence of specular reflection of solar radiation, or sun glint, may affect the measurement. To estimate the sun glint, the following model after Kay *et al.* [34] is employed:

$$\gamma_\lambda^s = (1 - W)\frac{E_\lambda \rho[\omega, \lambda] p[z_x, z_y]}{4\,\pi \cos^4 \beta} T_\lambda^{1-\cos\theta_s \sec\theta_v} \tag{9}$$

W is the fractional area covered by foam, E_λ is the extra-atmospheric solar irradiance, $\rho(\omega,\lambda)$ is the Fresnel reflection coefficient of the water surface for the given solar and sensor geometry, $p(z_x,z_y)$ is the probability of a given surface element having the required surface slope to specularly reflect light from the sun into the detector, θ_s is the solar zenith angle, and θ_v, is the sensor viewing angle. The ω and β are angular measures accounting for the geometry of the sun and sensor, given the azimuths of the sun, φ_s, and sensor, φ_v:

$$\cos^2 \omega = \tfrac{1}{2}(\sin\theta_s \sin\theta_v \cos(\varphi_s - \varphi_v) + \cos\theta_s \cos\theta_v + 1) \tag{10a}$$

$$\cos\beta = \frac{\cos\theta_s + \cos\theta_v}{2\,\cos\omega}. \tag{10b}$$

Kay *et al.* [34] provide the Cox and Munk [29] expression for $p(z_x,z_y)$ as well as a more recent version by Bréon and Henriot [30] which presents coefficients with reduced uncertainty. In this study, the version of Bréon and Henriot is used.

In the absence of foam, sun glint, while dependent on wind speed through the probability density function for wave slopes, is relatively insensitive to wind speeds over the normal range, changing only by 0.3% between 0 and 30 m/s. The error in the scattering estimate caused by sun glint is also very low compared with the intensity of the lidar backscattering, because only approximately 0.006% of the sun's energy falls within the bandwidth of the CALIOP detector. In the presence of foam, the sun glint falls off as the wind speed increases because less glint is possible from foam-covered slopes. This model assumes that foam is distributed over the surface in a pattern uncorrelated with water surface slope. Even in the case where this assumption is invalid, the estimated sun glint for 3.7 m/s represents an upper bound on the sun glint for wind speeds greater than this value, as it represents a foamless case. For winds less than 3.7 m/s, this assumption is not necessary as foam is assumed to be absent.

The sun glint model is relatively insensitive to uncertainty in the parameters. Using published [30] uncertainties in the parameters for the wave slope probability, and 10% uncertainties in the parameters of the foam model as above, the model exhibits at most 3% error in the predicted sun glint.

2.5. Sunlit Foam

Sunlit foam also is modeled as a Lambertian scatterer. Using a method similar to Moore *et al.* [32], scattering is modeled as an additional scattering term dependent upon the foam reflectance:

$$\gamma_\lambda^{sf} = W\left(\frac{1}{1-W}\gamma_\lambda^s + RSAR_\lambda \frac{\cos\theta_s}{\cos\theta_v}\frac{E_\lambda \Omega A \cos\theta_v}{I\, t_p} T_\lambda^{1-\cos\theta_s \sec\theta_v}\right) \quad (11)$$

The first term in Equation (13) represents the surface return in the absence of foam, while the second term represents the additional scattering due to foam. W and γ_λ^s have been previously defined in Equations (5) and (11), respectively. $RSAR_\lambda$ is the additional foam reflectance, either Equation (6) or (8) depending on wavelength, E_λ is the extra-atmospheric solar irradiance, Ω is the solid angle of the lidar detector, A is the area of the ground spot, I is the laser energy, t_p is the pulse length, and T_λ is the atmospheric transmittance along the lidar look direction. See Table 1 for the lidar-specific parameters applicable to CALIOP. The only wind-speed dependence for this term is the areal coverage of the foam. For all wind speeds less than 30 m/s, the foam contribution is an order of magnitude less than the sun glint.

Table 1. CALIOP lidar-specific parameters for Equation (13).

Parameter	Value	Note
Ω	1.26×10^{-13} sr	
A	3.85×10^{3} m^2	
I	1.1×10^{-1} J	
t_p	2.0×10^{-8} s	
θ_v	5.236×10^{-3} (0.3°)	(June 2006–November 2007)
	5.236×10^{-2} (3.0°)	(November 2007–)

The sensitivity to model parameters in the sunlit-foam model is dependent on wind speed. The parameters of the sunlit foam model are the same as those of the lidar foam model, and relate to the coverage and reflectance of the foam. However, the sunlit-foam model is less affected by the model parameters than the lidar foam model. At low-to-moderate wind speeds, the model is fairly insensitive to the model parameters, with uncertainties less than a factor of two for wind speeds less than about 22 m/s.

2.6. Subaqueous Scattering

The full model for subaqueous scattering (γ^{u}_{532}) is obtained by rewriting Equation (1) and combining with Equation (4), or:

$$\gamma^{u}_{532} = \frac{\gamma_{532}}{T_{532}} - \left(\frac{\rho_{532}}{\rho_{1064}}\left(\frac{\gamma_{1064}}{T_{1064}} - \gamma^{f}_{1064} - \gamma^{s}_{1064} - \gamma^{sf}_{1064}\right) + \gamma^{f}_{\lambda} + \gamma^{s}_{\lambda} + \gamma^{sf}_{\lambda}\right) \tag{12}$$

Further combining Equation (14) with Equations (6, 8, 10, 11 and 13) yields the expanded form:

$$\begin{aligned}
\gamma^{u}_{532} = \frac{\gamma_{532}}{T_{532}} & \\
& - \left(\frac{\rho_{532}}{\rho_{1064}} \left(\frac{\gamma_{1064}}{T_{1064}} \right. \right. \\
& - \left(W \left(\frac{\rho_{1064}}{4\,\pi\,\sigma^2 \cos^4\theta} \exp\left[\frac{-\tan^2\theta}{2\sigma^2}\right] + A[U] \exp\left[-1064k[\mathrm{U}]\right] \frac{\cos\theta}{\pi} \right) \right) \\
& - \left((1-W) \frac{E_{1064}\rho[\omega,1064]p[z_x,z_y]}{4\,\pi\cos^4\beta} T_{1064}^{1-\cos\theta_s \sec\theta_v} \right) \\
& - \left(W \left(\frac{E_{\lambda}\rho[\omega,1064]p[z_x,z_y]}{4\,\pi\cos^4\beta} T_{1064}^{1-\cos\theta_s \sec\theta_v} \right) \right. \\
& \left. \left. + W(A[U]\exp\left[-1064k[U]\right]) \frac{\cos\theta_s}{\cos\theta_v} \frac{E_{1064}\Omega A \cos\theta_v}{I\ t_p} T_{1064}^{1-\cos\theta_s \sec\theta_v} \right) \right) \\
& + \left(W \left(\frac{\rho_{532}}{4\,\pi\,\sigma^2\cos^4\theta} \exp\left[\frac{-\tan^2\theta}{2\sigma^2}\right] + 3.14 \times 10^{-6} U^{2.55} \frac{\cos\theta}{\pi} \right) \right) \\
& + \left((1-W) \frac{E_{532}\rho[\omega,532]p[z_x,z_y]}{4\,\pi\cos^4\beta} T_{532}^{1-\cos\theta_s \sec\theta_v} \right) \\
& + \left(W \left(\frac{E_{532}\rho[\omega,532]p[z_x,z_y]}{4\,\pi\cos^4\beta} T_{532}^{1-\cos\theta_s \sec\theta_v} \right) \right. \\
& \left. \left. + W\,(3.14 \times 10^{-6} U^{2.55}) \frac{\cos\theta_s}{\cos\theta_v} \frac{E_{532}\Omega A \cos\theta_v}{I\ t_p} T_{532}^{1-\cos\theta_s \sec\theta_v} \right) \right)
\end{aligned} \tag{13}$$

For nighttime overpasses, sun glint and sunlit foam in both wavelengths are zero simplifying to:

$$\gamma_{532}^{u} = \frac{\gamma_{532}}{T_{532}} - \left(\frac{\rho_{532}}{\rho_{1064}} \left(\frac{\gamma_{1064}}{T_{1064}} - \left(W\left(\frac{\rho_{1064}}{4\,\pi\,\sigma^2 \cos^4\theta} \exp\left[\frac{-\tan^2\theta}{2\sigma^2} \right] + A[U] \exp\left[-1064k[\mathrm{U}] \right] \frac{\cos\theta}{\pi} \right) \right) \right) + \left(W\left(\frac{\rho_{532}}{4\,\pi\,\sigma^2 \cos^4\theta} \exp\left[\frac{-\tan^2\theta}{2\sigma^2} \right] + 3.14 \times 10^{-6} U^{2.55} \frac{\cos\theta}{\pi} \right) \right) \right) \quad (14)$$

2.7. Comparison of Backscatter Terms

Figure 3 shows model results for the magnitude of the components of the total integrated attenuated backscatter without subsurface scattering, to give a sense of the relative importance of each term. A solar zenith angle of 30° is assumed. The specular wave scattering shown is from Equation (2), in contrast to the method outlined in Section 2.2 to allow a theoretical dependence on wind speed for comparison to the other terms. In the case study presented in Section 3, subsurface scattering ranged from 0.0 to 0.13 sr^{-1}.

Figure 3. Theoretical CALIOP scattering off water surface as a function of wind speed for 532 and 1064 nm wavelengths. Wave scattering is modeled using Equation (2). Foam scattering and sun-on-foam are modeled by Equation (10). Sun glint is modeled as Equation (11). Graphs illustrate the relative importance of the different components to the total integrated scattering. The solar zenith angle is assumed to be 30°.

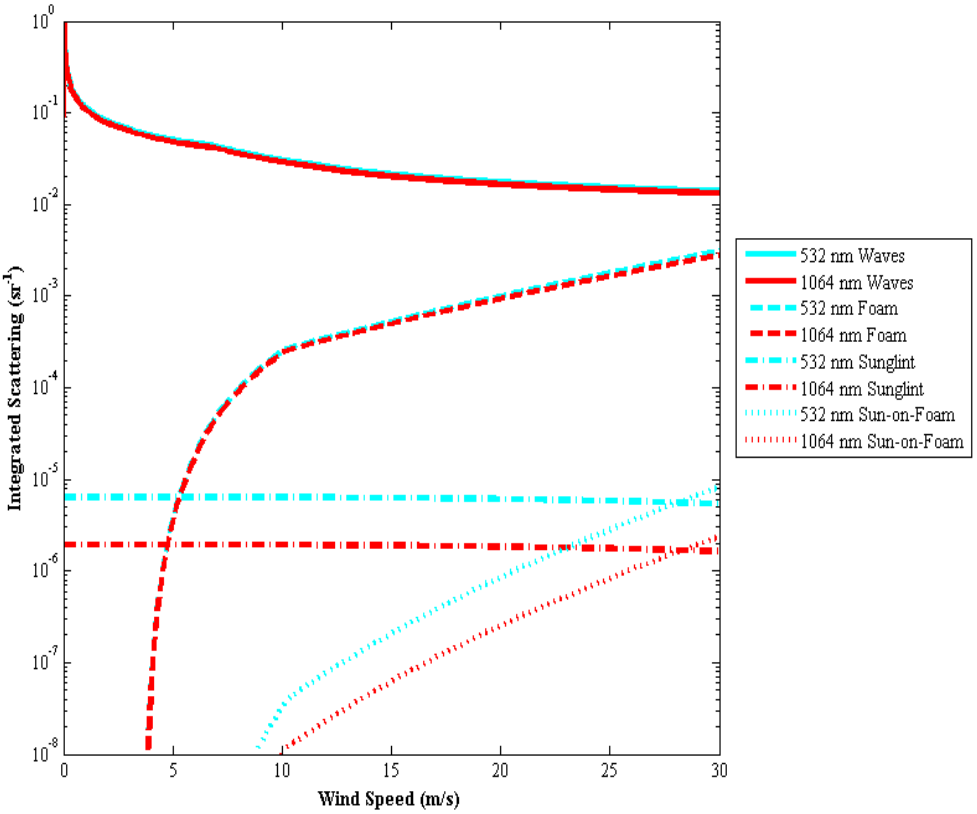

2.8. Uncertainties

Uncertainty propagation analysis allows the evaluation of the sensitivity of the model to input error. There are five major inputs into the model: First, an estimate of wind speed is required to estimate the foam component. Second, transmittances are needed for both the green and the infrared channels. Third, the total integrated attenuated backscatter from the lidar measurements is needed in both green and infrared. Uncertainty is introduced both during the measurement process and also during any numerical integration with depth.

2.8.1. Wind Speed Estimate

The use of Equation (4) instead of Equation (2) for the specular surface return results in a modeled subaqueous integrated backscatter that is relatively insensitive to the wind speed estimate. Figure 4 shows this lack of sensitivity, which even at very high wind speeds never exceeds 0.002 s m^{-1} sr^{-1}.

Figure 4. Error in subaqueous integrated backscatter due to 1 m/s overestimate in wind speed estimate. Because the wind speed estimate is only used to estimate foam cover and reflectance, the error at low wind speeds is negligible.

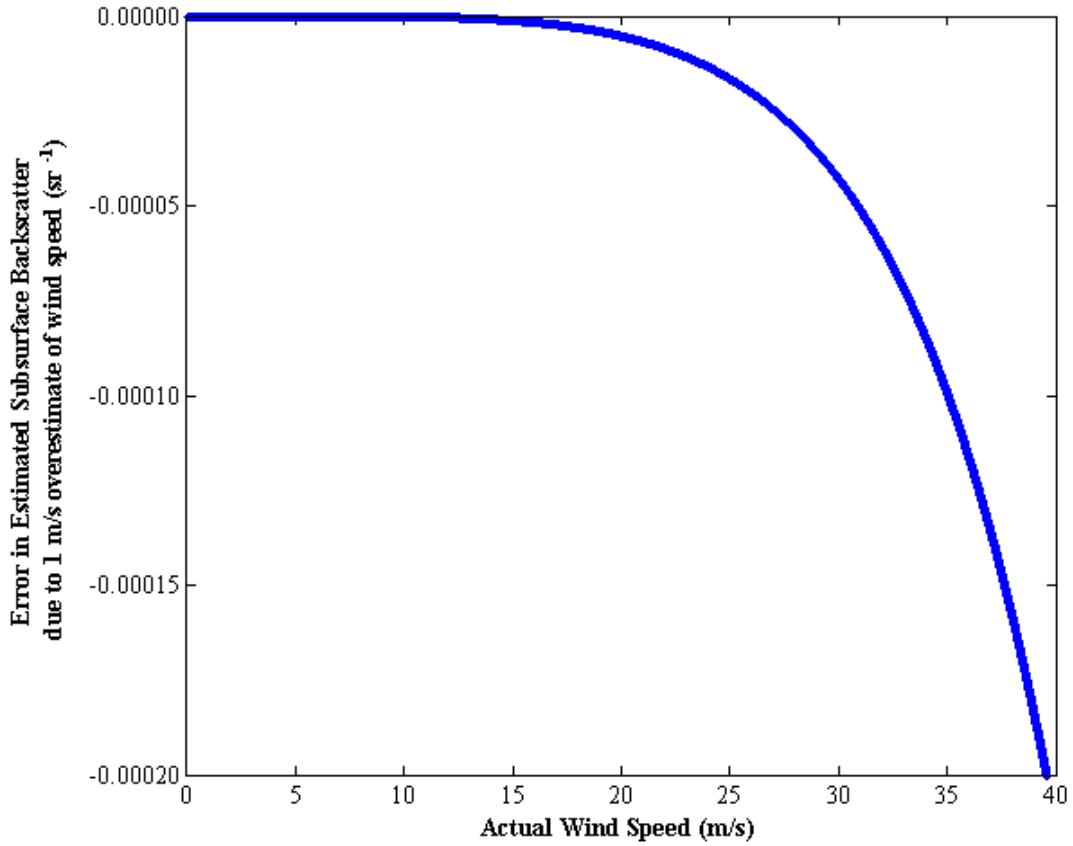

2.8.2. Transmittance Estimate

Two transmittance estimates are used in the atmospheric correction of the lidar data; at 532 nm and at 1,064 nm. The accuracies of these estimates are important considerations in determining the accuracy of the subaqueous integrated backscatter estimate. From Equation (15), it can be shown that:

$$\frac{\partial \gamma_{532}^{u}}{\partial T_{532}} = -2\frac{\gamma_{532}}{T_{532}^{3}} \tag{15a}$$

$$\frac{\partial \gamma_{532}^{u}}{\partial T_{1064}} = 2\frac{\rho_{532}}{\rho_{1064}}\frac{\gamma_{1064}}{T_{1064}^{3}} \tag{17b}$$

Equation (17) shows that the sensitivity to the transmittance increases linearly with the total backscatter. Figure 5 shows the dependence upon both the total integrated backscatter and the transmittance. It is clear from both Equation (17) and from Figure 5 that the accuracy of the transmittance estimate plays an important role in determining the uncertainty of the final result, and that low transmittance data may provide largely meaningless results.

Because of the opposing signs of (17a) and (17b), positively correlated errors in T_{532} and T_{1064} will tend to cancel. This will tend to limit the error introduced by the surface visibility parameter to the model.

Figure 5. Error in subaqueous integrated backscatter due to 0.01 overestimate in the 532 nm transmittance estimate. The error due to an overestimate in the 1064 nm transmittance is proportional, with a constant of proportionality of $-\rho_{1064}/\rho_{532} \approx -0.9494$. The error is dependent upon the total integrated backscatter received; the two curves represent low (0.01 sr^{-1}, blue) and high (0.1 sr^{-1}, red) integrated backscatters.

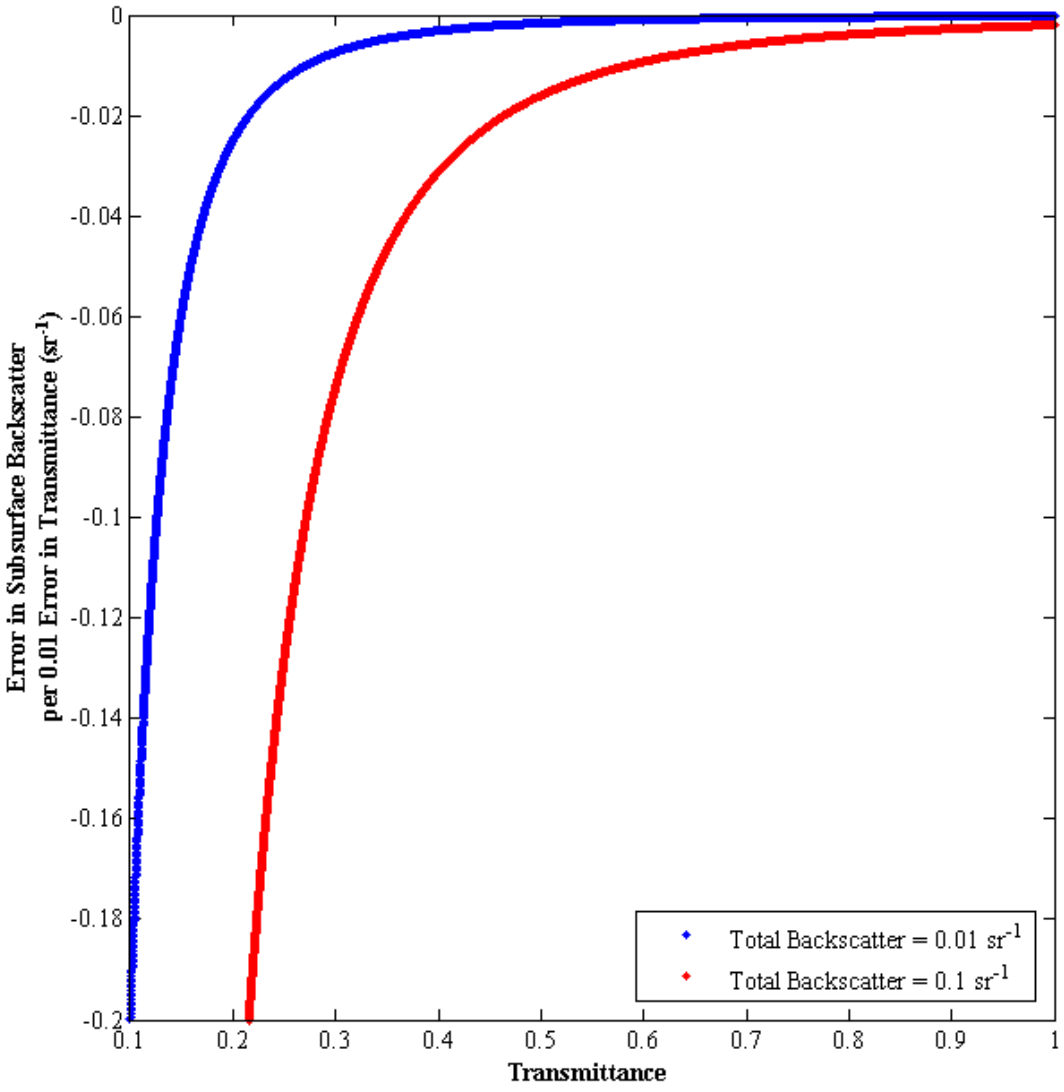

2.8.3. Integrated Backscatter

The attenuated backscatter measured by the lidar sensor is numerically integrated to obtain the total integrated attenuated backscatter. There is uncertainty associated both with the original attenuated backscatter measurements and with the numerical integration scheme used. The sensitivity of the model to these uncertainties can be summarized by the following:

$$\frac{\partial \gamma^{u}_{532}}{\partial \gamma_{532}} = T^{-2}_{532} \tag{16a}$$

$$\frac{\partial \gamma^{u}_{532}}{\partial \gamma_{1064}} = -\frac{\rho_{532}}{\rho_{1064}} T^{-2}_{1064} \tag{18b}$$

Like the sensitivity to the transmittance, the sensitivity to the total integrated attenuated backscatter is dependent on the transmittance (Figure 6). The error in the subaqueous integrated backscatter is always greater than the error in the total integrated attenuated backscatter, and is greater by more than a factor of four for transmittances less than 0.5. This sensitivity makes the accuracy of the total integrated attenuated backscatter input at least as important as the accuracy of the transmittance estimate in determining the uncertainty in the final result.

Figure 6. Error in the subaqueous integrated backscatter for a 0.001 sr^{-1} error in the total integrated attenuated backscatter. This level of uncertainty was observed in the CALIOP data when comparing different numerical integration schemes. The errors associated with uncertainties in both bands are shown.

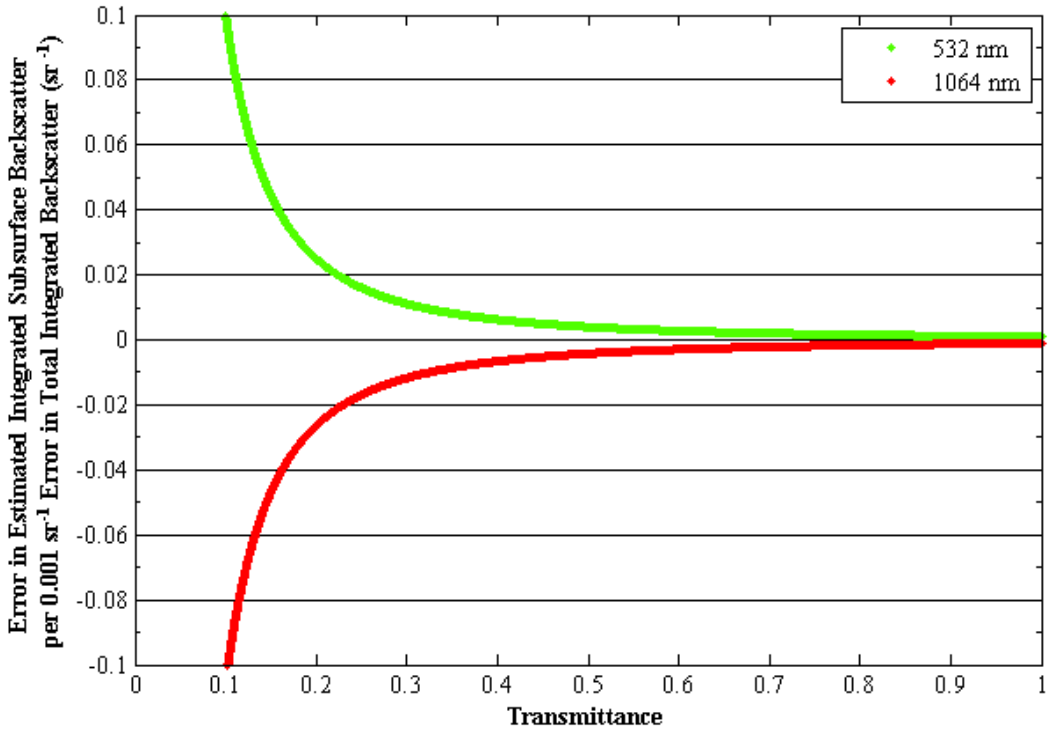

As for the transmittances, the opposing signs (and roughly equal magnitude; $\rho_{532}/\rho_{1064} \approx 1.053$) of (18a) and (18b) will cause the effects of positively correlated errors in γ_{532} and γ_{1064} to cancel. This should help to ameliorate the effect of the choice of numerical integration scheme, which might introduce systematic errors.

3. Case Study: Tampa Bay, Florida, USA

3.1. Site Description

Tampa Bay is located on the west coast of the Florida Peninsula between 27.3–28.1°N and 82.4–82.8°W, as shown in Figure 7. Fresh water inflow to the bay comes from a watershed of about 596,000 km^2 [35] through four major rivers: the Hillsborough River, the Alafia River, the Little Manatee River, and the Manatee River. Chen *et al.* [15] found that the Alafia and the Hillsborough dominate the delivery of dissolved organic carbon (CDOM) to the bay, and also found that CDOM is the primary absorber at blue wavelengths in the estuary. Lewis and Whitman [36] identified seven major segments of Tampa Bay: Old Tampa Bay, Hillsborough Bay, Middle Tampa Bay, Lower Tampa Bay, Boca Ciega Bay, Terra Ceia Bay, and Manatee River. In general, sediment size increases as one progresses from Hillsborough Bay through the Lower Tampa Bay. Old Tampa Bay is heterogeneous though generally it coarsens toward the outlet. Terra Ceia and the Manatee River estuary are characterized by medium to fine sands. Boca Ciega Bay contains fine sand to mud, generally coarsening to the south [37]. The Environmental Protection Commission of Hillsborough County (EPCHC) samples turbidity and other water quality parameters at 56 fixed stations in Tampa Bay once per month, on a rotating schedule.

3.2. Data

Data from the CALIOP lidar were combined with reflectance data from the MODIS radiometer. Surface wind speed and visibility data, from airports and buoys, along with atmospheric data provided with the CALIOP data were used to construct a LOWTRAN model.

3.2.1. CALIOP Data

CALIPSO, the satellite upon which the CALIOP lidar resides, was launched on 28 April 2006. Seven overpasses were selected between that date and the late November 2007 pitch maneuver that changed the zenith angle of CALIOP from 0.3° to 3.0°. The seven overpasses selected for evaluation were chosen based on absence of cloud cover. The descending pass of CALIOP is the only pass that traverses the bay which forced the use of solely nighttime scenes. Version 3 CALIOP data were used except where noted.

Four data products were used in this analysis. The Level 1 product provides backscatter data as a function of altitude. For altitudes below sea-level, the altitudes were corrected for the speed of light in seawater compared to air, and the resulting function of altitude was numerically integrated using a trapezoidal scheme over the interval from the surface bin through five bins below the surface. Low-pass filtering inherent in the CALIOP electronics causes the analog-to-digital conversion to smear the surface return into subsequent bins, so this integration is necessary, although these five bins represent a depth of water from which it is unreasonable to expect real returns [24].

The Level 2 Cloud and Aerosol Layer products were used to provide the optical depths and the altitudes of the tops and bottoms of the atmospheric strata. Shots that were flagged as containing opaque layers or other quality problems were rejected from the analysis. The Level 2 Atmospheric

Profile Version 2 beta product was used only to provide temperature, pressure, ozone, and molecular profile data, all provided by the NASA Global Modeling and Assimilation Office (GMAO), which was then used as input into a LOWTRAN model.

3.2.2. MODIS Data

Terra-MODIS Level 2 (MOD09QK) surface reflectance (normalized radiance) products were retrieved from the LPDAAC corresponding to the afternoon before each CALIPSO overpass. The Terra overpass was a compromise of the closest overpass in time and the closest to nadir observation. After geocoding, the data located over Tampa Bay were extracted. The normalized radiance values (ρ) were converted to remote-sensing reflectances (R_{RS}), assuming that the illumination can be approximated as isotropic:

$$R_{RS} = \frac{\rho}{\pi} \tag{17}$$

3.2.3. Supplementary Data

Historical meteorological data were obtained from seven airports and four buoys situated in and around the bay. The airports were: Tampa International Airport (TPA) [27°58′32″N, 82°32′0″W], Peter O. Knight Airport (TPF) [27°54′56″N, 82°26′57″W], MacDill Air Force Base (MCF) [27°50′57″N, 82°31′15″W], Tampa Executive Airport (VDF) [28°00′50″N, 82°20′43″W], St. Petersburg/Clearwater International Airport (PIE) [27°54′36″N, 82°41′15″W], Albert Whitted Airport (SPG) [27°45′54″N, 82°37′36″W], Sarasota/Bradenton International Airport (SRQ) [27°23′44″N, 82°33′15″W]. These airports record hourly measurements of wind speed and visibility. The several Coastal-Marine Automated Network (CMAN) buoys that provide six- to twenty-minute wind speed data are Egmont Key (EGKF1) [27°36′3.6″N, 82°45′36″W], Anna Maria Island (ANMF1) [27°33′0″N, 82°45′0″W], Port Manatee (PMAF1) [27°38′13″N, 82°33′47″W], and Clearwater Beach (CWBF1) [27°58′36″N, 82°49′54″W], which provided data for this study. The locations of these ground stations within the topobathymetric setting of the estuary are shown in Figure 7.

Depths were acquired from the NOAA National Geophysical Data Center (NGDC) Coastal Relief products, combined with gridded airborne lidar depth soundings from the Experimental Advanced Airborne Research Lidar (EAARL) in some shallow waters; these data were also acquired from the NGDC. The EAARL data are limited to depths shallower than three meters, and are not spatially extensive. These depth data were gridded together at approximately 3.67 m posting, as this was the posting of the processed lidar dataset, to obtain seamless bathymetry of the bay. In most cases, however, the resolution of the depth data is significantly less than this posting.

Although Tampa Bay has a strong history of *in situ* turbidity research, there are no data both coincident and contemporaneous with the lidar coverage in the period of study. Although the small 90 m lidar spot size is an advantage when considering spatial heterogeneity, it becomes a liability when attempting to find fortuitous matches with established study sites. Over the period between June 2006 and October 2007, there were no study sites within 1 km of any overpass that were occupied within two days of the overpass.

Figure 7. Topobathymetry of Tampa Bay. Bathymetry in purple is derived from an airborne lidar survey in May 2007 [38]; topography and bathymetry in blue is a composite of NOAA GEODAS and the Global Multi-Resolution Topography product [39]. Also shown are the seven airports and four CMAN buoys from which wind speed and/or visibility data were obtained. The map is shown in a latitude-longitude pseudoprojection, with northwest corner [28°04′26.546304″N, 82°52′08.082264″W], and southeast corner [27°19′58.28718″N, 82°19′58.004148″W].

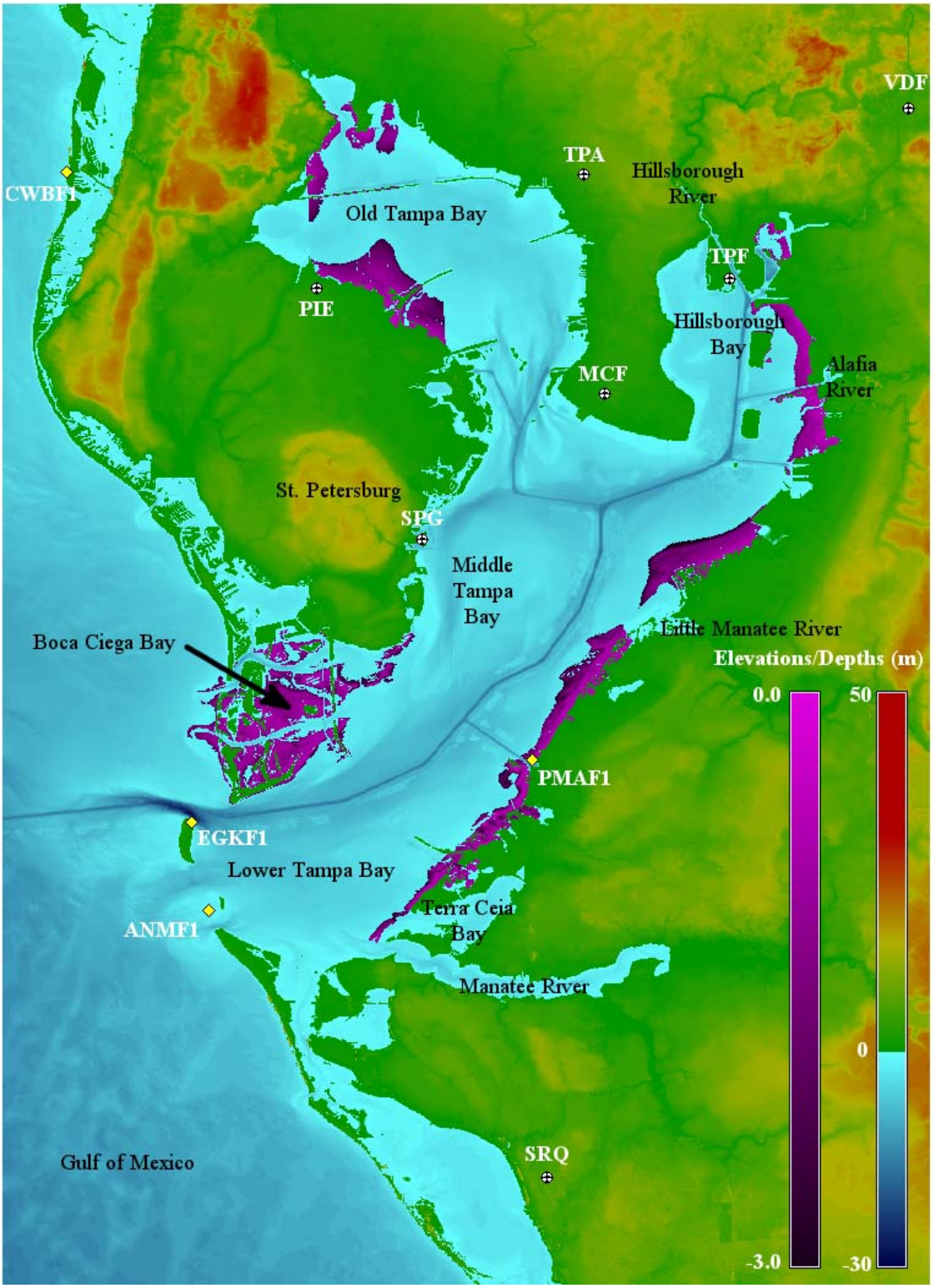

3.3. Analysis

The data were processed through the algorithm described above. Wind speeds were estimated by interpolation from records collected at the airports and buoys shown in Figure 7. Surface visibility, a parameter in the clear-air LOWTRAN model, was also interpolated from airport records. A sensitivity analysis was carried out on the effect of these inputs, and it was found that changing the wind speed by 90% and the visibility by 50% had a nearly undetectable result on the resulting subaqueous integrated backscatter. This is due to the wind speed estimate affecting only the foam reflectance, which is small, and the visibility affecting only the clear-air optical depth, which represents only a very small fraction of the total atmospheric optical depth. It is likely that at very high wind speeds or very low visibilities, beyond the range of those seen in this study, these sensitivities would increase.

Fourteen points were identified as outliers, using Peirce's criterion, as outlined in the work of Ross [40]. All of these points had estimated γ_u values above 1.0 sr^{-1}, more than six times the largest non-outlier. All of these points were acquired on 07 May 2007, a date which had relatively low atmospheric transmittance.

Although there are no coincident *in situ* measurements of backscatter or turbidity with the CALIOP transects, Tampa Bay has been well studied as a venue for the use of MODIS 645 nm radiance and reflectance data for the estimation of turbidity. MODIS is a passive radiometer, which, in regions far from the specular solar disk, images mainly subsurface scattering and relatively low levels of foam and sun glitter from waves. Thus, in order to evaluate the capability of the CALIOP to detect subsurface scattering, a comparison was made of the CALIOP data with MODIS Channel 1 data. The justification is that the MODIS 645 nm band has been previous shown to be nearly linearly related to turbidity [14,15].

Still, there are important limitations to this comparison. Perhaps the most important is that the MODIS acquisitions require daylight, which imposes a minimum time separation between the MODIS acquisition and the CALIOP acquisition; for the seven days used, the Terra overpass from the afternoon before the CALIOP measurement was used for comparison. During daylight hours, the A-Train configuration of the Aqua and CALIPSO satellites could be exploited to derive nearly simultaneous measurements. Another limitation to this comparison is the unknown penetration depths for MODIS and CALIOP. Chen *et al.* [15] and Moreno-Madrinan *et al.* [41] showed that the MODIS Channel 1 (645 nm) remote sensing reflectance (R_{RS}) is well correlated with turbidity in Tampa Bay, for depths greater than about 2.5 m (Chen *et al.*: 2.8 m; Moreno-Madrinan *et al.*: 2.4 m). This suggests that the penetration depth for MODIS is in this range, and that for shallower waters, the bottom scattering becomes an important component to the total return. No previous work has investigated the penetration depth of CALIOP; this depth must depend upon the strength of the light, the sensitivity of the detector and the strength of the backscattering from the target, so it is not trivial to determine. An investigation of the correlation of CALIOP backscatter with MODIS reflectance showed no threshold depth in the relationship similar to those observed previously between MODIS reflectance and turbidity.

It would be preferable to compare the CALIOP data with field observations, as was done with the MODIS data by Chen *et al* and Moreno-Madrinan *et al*. However, the limited spatial extent makes this extremely difficult, as only up to five of the EPCHC field sites are within one kilometer of any CALIOP track. The time elapsed between measurements typically varies between two days and nine

days. Without a planned simultaneous observation campaign, such field validation is not feasible with a single-beam lidar.

Following Moreno-Madrinan *et al.* [41], the 250 m MOD09QK land surface reflectance product was used for the evaluation. For each CALIOP observation over water, the closest MOD09 grid cell was chosen which was entirely water. The NOAA Global, Self-consistent, Hierarchical, High-resolution Shoreline Database (GSHHS) [42] was used to identify pixels contaminated by land.

The seven paired CALIOP and MODIS datasets are shown in Table 2. Also shown are the correlation coefficients and significance p-values for each pair. The final row in the table shows the results of the analysis for all of the data combined.

Table 2. Paired CALIOP and MODIS observations of Tampa Bay from June, 2006 through November, 2007. Excluded from these analyses are fourteen points from 07 May 2007 that were identified by Peirce's criterion as outliers. (All of these had $\gamma_u > 1.0$ sr^{-1}).

Date/UTC Time of CALIOP Overpass	Number of Cloud-Free Shots	Mean Atmospheric Transmittance (Cloud-Free)	Date of Terra MOD09 (Daily) Product	Number of Cloud-Free Pairs of CALIOP/MODIS	Correlation Coefficient between CALIOP and MODIS (95% c.i.)	p-value
2006-08-08 07:21:50	144	0.66	2006-08-07	92	0.26 (0.12; 0.42)	1.8×10^{-7}
2006-09-25 07:17:41	148	0.65	2006-09-24	136	0.23 (0.11; 0.36)	3.4×10^{-9}
2007-05-07 07:23:10	140	0.46	2007-05-06	70	0.03 (0.002; 0.16)	1.2×10^{-1}
2007-05-23 07:24:13	160	0.61	2007-05-22	63	0.43 (0.24; 0.60)	5.7×10^{-9}
2007-07-10 07:24:00	147	0.66	2007-07-09	113	0.10 (0.02; 0.22)	8.2×10^{-4}
2007-09-28 07:16:58	153	0.70	2007-09-27	53	0.14 (0.01; 0.34)	6.6×10^{-3}
2007-10-14 07:14:53	143	0.68	2007-10-13	133	0.46 (0.33; 0.58)	2.7×10^{-19}
Aggregated Data	1035	0.64	Aggregated Data	660	0.11 (0.07; 0.16)	5.8×10^{-19}

3.4. Discussion

As an example, the MODIS R_{RS} of 13 October 2007, calculated from the MOD09 Land Surface Reflectance product, is shown in Figure 8, where the land is masked out and filled with topography. Superimposed on the MODIS reflectances are the CALIOP shot locations from the overpass of the early morning of 14 October 2007. Figure 9(a) shows the results of the subsurface backscatter algorithm along the CALIOP swath. The MODIS R_{RS} along the swath is shown in Figure 9(b). This corresponds to the data in Figure 8, along the CALIOP track. Figure 9(c) shows the depth profile along the track, as a reference for the other two plots. Four distinct zones have been identified on this plot; from south to north: Gulf of Mexico is the area southwest of Tampa Bay, offshore from Anna Maria

Island. It is characterized by low reflectance in the MODIS 645 nm channel. Lower Bay is the stretch of water between Anna Maria Island and Mullet Key, which is the mouth of the bay, spanning the outlet of the navigation channel. It is characterized by moderate to low reflectance in the MODIS 645 nm channel. Boca Ciega Bay is a region of shoals and grass beds between Mullet Key and the mainland, southwest of St. Petersburg. Boca Ciega Bay is characterized by high reflectance and high scatter in the 645 nm channel, and is characterized by extremely shallow waters (<4 m). Old Tampa Bay separates St. Petersburg from Tampa, and is characterized by shallow waters (<5 m) and can have a wide range of reflectance values, though when it has high reflectance, the values are more self-consistent than Boca Ciega Bay.

Figure 8. MODIS MOD09 derived 645 nm Remote Sensing Reflectance (R_{RS}) (shades of blue and cyan) for 13 October 2007 and the corresponding 14 October 2007 CALIOP shots (red dots). Land was masked using the NOAA Global Self-consistent, Hierarchical, High-resolution Shoreline Database (GSHHS). In this figure, it has been filled with the Global Multi-Resolution Topography Product. The very high values of R_{RS} along the shorelines are probably due to bottom reflection. The CALIOP footprints are shown larger than actual size for visibility.

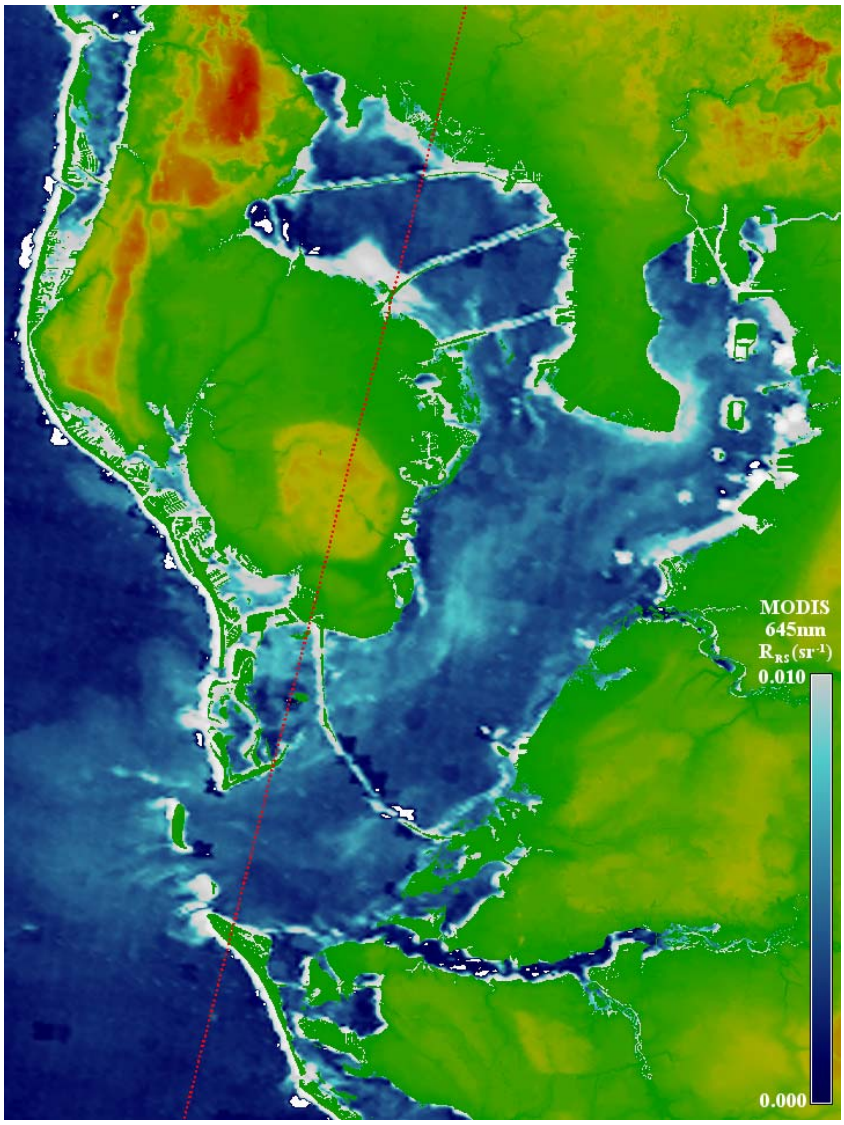

Figure 9. Transect across the Tampa Bay Region (see Figure 8 for location) following the 14 October 2007 CALIOP track. **(a)** CALIOP integrated subsurface backscatter (γ_u). **(b)** MODIS remote sensing reflectance (Channel 1: 645 nm). The MODIS data presented represents the closest MODIS grid cell to a CALIOP pixel which is free of land. **(c)** Transect of elevation/depth along the CALIOP track, relative to the NAVD datum.

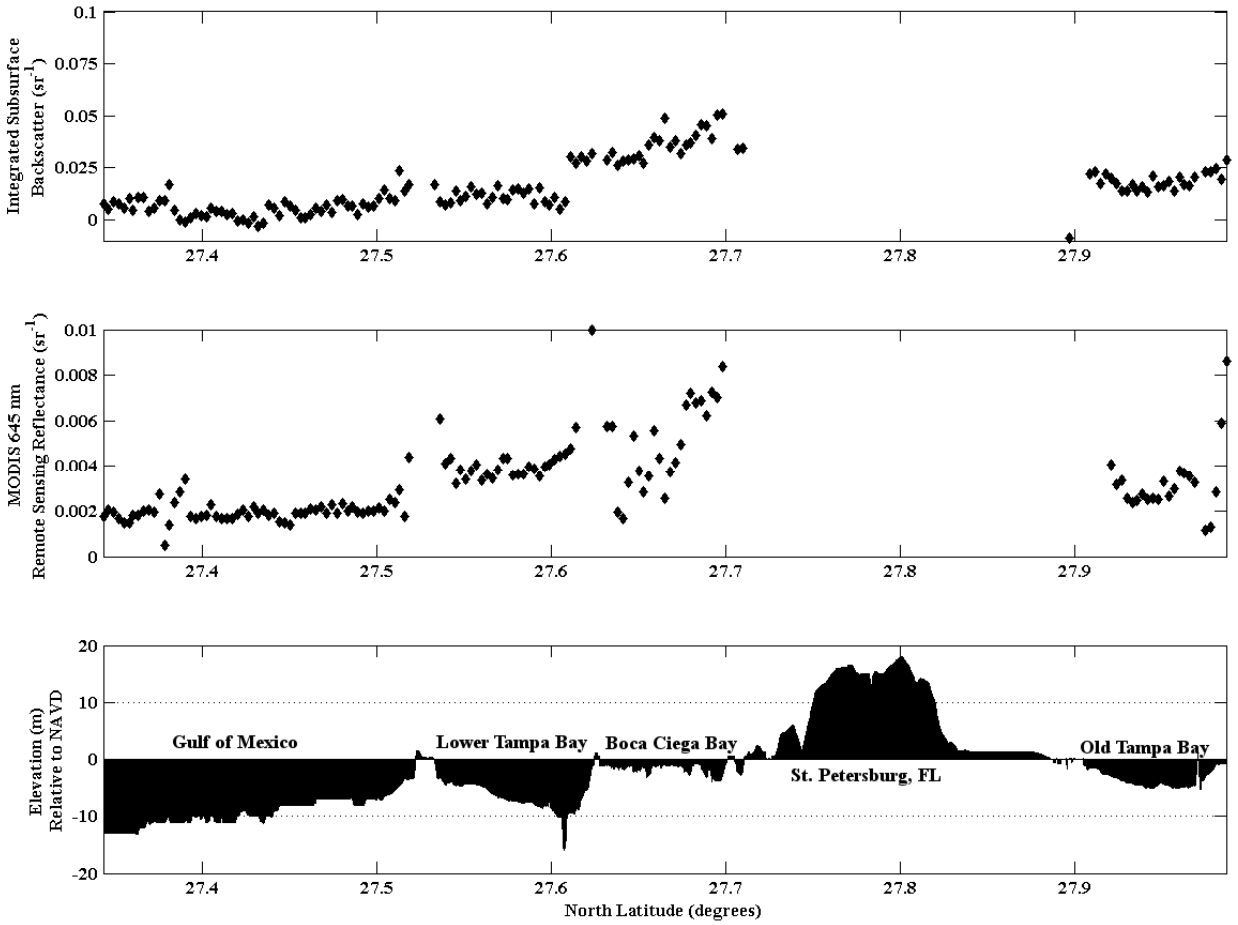

Figure 10 is a scatterplot of the collected CALIOP integrated backscatter, γ_u, *versus* the MODIS 645 nm remote sensing reflectance, R_{RS}. Although the correlation of 0.11 is low, its p-value shows a remarkably high level of significance. It is clear that in the mean, the CALIOP and the MODIS data are responding to similar phenomena.

4. Conclusions

A theoretical method has been presented for estimating subaqueous integrated backscatter from the near-nadir viewing satellite lidars such as CALIOP. External inputs to the algorithm are principally wind speed and surface visibility. The algorithm takes into account specular reflection of laser light at the water surface, laser scattering by wind-generated foam as well as sun glint and solar scattering from the foam. An important feature of the algorithm is the use of the infrared backscattering as a basis for predicting the specular green backscattering. This allows the implicit correction for water surface geometry that may not follow simplistic model assumptions.

Figure 10. Scatter plot of CALIOP 532 nm integrated subsurface backscatter and MODIS 645 nm remote sensing reflectance. The Pearson's correlation coefficient is 0.11. The exceptionally low points ($\gamma_u < -0.05$ sr^{-1}) are all from 07 May 2007, from points of low transmittance. Fourteen outliers identified with Peirce's criterion with $\gamma_u > 1.0$ sr^{-1} are not shown.

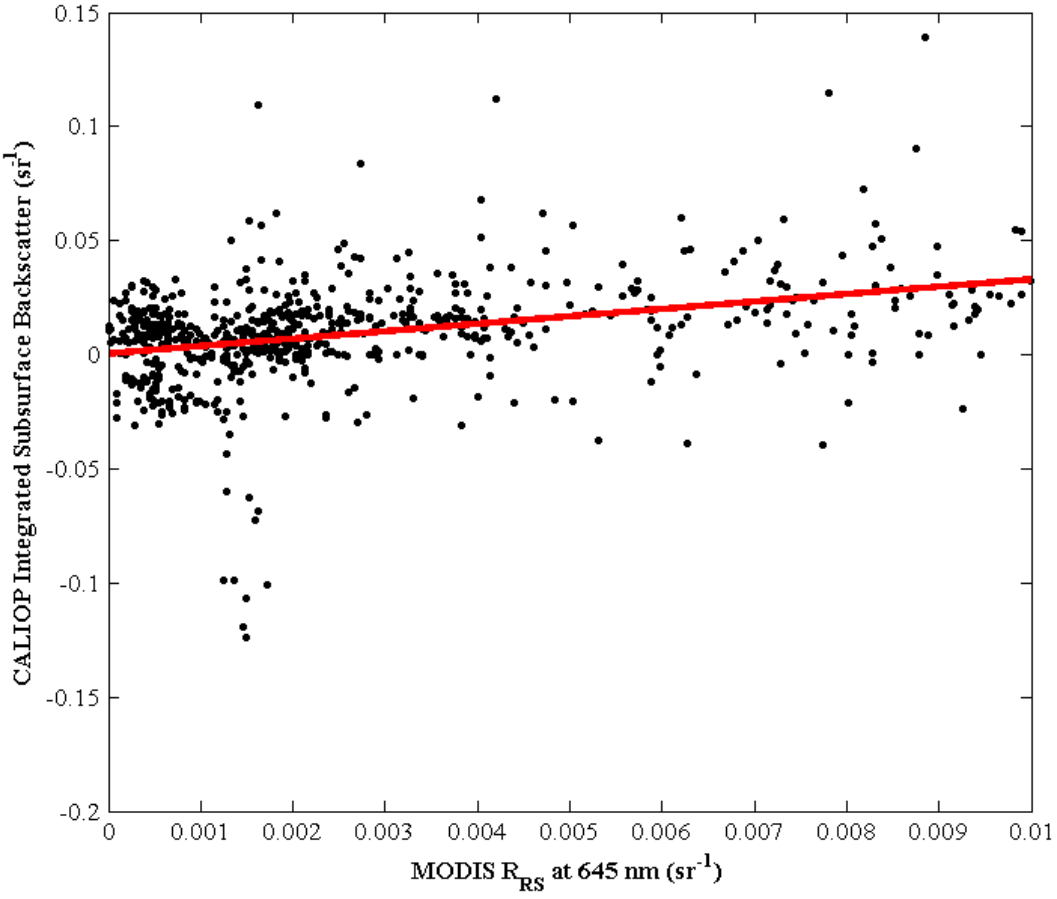

Theoretical analysis indicates that the model is insensitive to wind speed, but relatively sensitive to errors in atmospheric transmittance and total integrated attenuated backscatter. However, errors in the transmittance or total attenuated integrated backscatter that are positively correlated between the two bands will tend to cancel out because of the reversed sign of the sensitivity.

In a case study, the method was applied to nighttime CALIOP data over Tampa Bay, using interpolated wind speed and visibility data from airports and buoys, and comparison was made to MODIS 645 nm remote sensing reflectance. Good correlation was found on six of seven dates with relatively high atmospheric transmittances, although the correlation decreases when data were composited over all dates. Results were found to be very insensitive to the wind speed and visibility inputs as predicted. The implication is that the 532 channel responds differently to the seasonally varying biogeochemical scatterers in the water column. Thus, while the single CALIOP 532 total integrated attenuated backscatter contains information about the subsurface, more channels may be needed to capture the full range of scattering affecting turbidity, at least within Tampa Bay. CALIOP was designed to measure principally optical properties of the atmosphere, but the current analysis indicates a potential for extracting subsurface scattering and turbidity as well.

Acknowledgements

This research was supported by the NASA Terrestrial Hydrology Program and also the NASA Postdoctoral Program administered by Oak Ridge Associated Universities. CALIOP data were obtained from the NASA Langley Research Center Atmospheric Science Data Center. MODIS data were obtained from the USGS Land Process Distributed Active Archive Center.

References

1. US Environmental Protection Agency. *National Water Quality Inventory—2000 Report*; EPA: Washington, DC, USA, 2002.
2. Klemas, V.; Borchardt, J.F.; Treasure, W.M. Suspended sediment observations from erts-1. *Remote Sens. Environ.* **1973**, *2*, 205-221.
3. Williams, R.S., Jr. Coastal and submarine features on MSS imagery of Southeastern Massachusetts: Comparison with conventional maps. In *Symposium of Significant Results from ERTS-1*; Goddard Space Flight Center: Greenbelt, MD, USA, 1973; pp. 1413-1422.
4. Hart, J. Remotely-sensed distributions of suspended sediment concentration in Lake Pontchartrain. *Trans. GCAGS* **1978**, *28*, 185-192.
5. Munday, J.C.; Alföldi, T.T. Landsat test of diffuse reflectance models for aquatic suspended solids measurement. *Remote Sens. Environ.* **1979**, *8*, 169-183.
6. Gordon, H.R. Simple calculation of the diffuse reflectance of the ocean. *Appl. Optics* **1973**, *12*, 2804-2805.
7. Gordon, H.R.; Brown, O.B.; Jacobs, M.M. Computed relationships between the inherent and apparent optical properties of a flat homogeneous ocean. *Appl. Opt.* **1975**, *14*, 417-427.
8. Gordon, H.R.; Brown, O.B. Irradiance reflectivity of a flat ocean as a function of its optical properties. *Appl. Opt.* **1973**, *12*, 1549-1551.
9. Curran, P.J.; Novo, E.M.M. The relationship between suspended sediment concentration and remotely sensed spectral radiance: A review. *J. Coast. Res.* **1988**, *4*, 351-368.
10. Stumpf, R.P.; Pennock, J.R. Remote estimation of the diffuse attenuation coefficient in a moderately turbid estuary. *Remote Sens. Environ.* **1991**, *38*, 183-191.
11. Chen, Z.; Curran, P.J.; Hansom, J.D. Derivative reflectance spectroscopy to estimate suspended sediment concentration. *Remote Sens. Environ.* **1992**, *40*, 67-77.
12. Gomez, B.; Mertes, L.A.K.; Phillips, J.D.; Magilligan, F.J.; James, L.A. Sediment characteristics of an extreme flood; 1993 upper mississippi river valley. *Geology* **1995**, *23*, 963-966.
13. Binding, C.E.; Bowers, D.G.; Mitchelson-Jacob, E.G. Estimating suspended sediment concentrations from ocean colour measurements in moderately turbid waters: The impact of variable particle scattering properties. *Remote Sens. Environ.* **2005**, *94*, 373-383.
14. Binding, C.E.; Bowers, D.G.; Mitchelson-Jacob, E.G. An algorithm for the retrieval of suspended sediment concentrations in the Irish sea from seawifs ocean colour satellite imagery. *Int. J. Remote Sens.* **2003**, *24*, 3791-3806.
15. Chen, Z.; Hu, C.; Muller-Karger, F. Monitoring turbidity in tampa bay using modis/aqua 250-m imagery. *Remote Sens. Environ.* **2007**, *109*, 207-220.

16. Tikhomirov, A.A. Results of ocean surface remote sensing with spaceborne lidar balkan from the space station MIR. *Proc. SPIE* **1999**, *3707*, 533-540.
17. Gordon, H.R. Interpretation of airbone oceanic lidar: Effects of multiple scattering. *Appl. Opt.* **1982**, *21*, 2996-3001.
18. Phillips, D.M.; Abbot, R.H.; Penny, M.F. Remote sensing of sea water turbidity with an airborne laser system. *J. Phys. D: Appl. Phys.* **1984**, *17*, 1749-1758.
19. Ivanov, A.P.; Kalinin, I.I.; Kolesnik, A.I.; Bondarenko, P.P. Features of the measurement of the extinction and absorption coefficients of water by pulsed probing. *J. Appl. Spectrosc.* **1978**, *29*, 1251-1257.
20. Phillips, D.M.; Scholz, M.L.; Abbot, R.H. *Water Turbidity Measurements in Gulf St. Vincent*; Technical Report; ERL-186-TR; Electronics Research Laboratory, Department of Defence: Salisbury, Australia, 1981; p. 23.
21. Billard, B. Remote-sensing of scattering coefficient for airborne laser hydrography. *Appl. Optics* **1986**, *25*, 2099-2108.
22. Preisendorfer, R.W. *Hydrologic Optic*; US Department of Commerce, NOAA: Honolulu, HI, USA, 1976.
23. Lancaster, R.S.; Spinhirne, J.D.; Palm, S.P. Laser pulse reflectance of the ocean surface from the glas satellite lidar. *Geophys. Res. Lett.* **2005**, *32*, L22S10.
24. Hu, Y.; Stamnes, K.; Vaughan, M.; Pelon, J.; Weimer, C.; Wu, D.; Cisewski, M.; Sun, W.; Yang, P.; Lin, B.; *et al*. Sea surface wind speed estimation from space-based lidar measurements. *Atmos. Chem. Phys.* **2008**, *8*, 3593-3601.
25. Kidder, S.Q.; Kankiewicz, J.A.; Vonder Haar, T.H. The A-Train: How Formation Flying is Transforming Remote Sensing. In *Proceedings of The Joint 2007 EUMETSAT Meteorological Satellite Conference and the 15th American Meteorological Society Satellite Meteorology and Oceanography Conference*, Amsterdam, The Netherlands, 24–28 September 2007.
26. Platt, C.M.R. Lidar and radioinetric observations of cirrus clouds. *J. Atmos. Sci.* **1973**, *30*, 1191-1204.
27. Menzies, R.T.; Tratt, D.M.; Hunt, W.H. Lidar in-space technology experiment measurements of sea surface directional reflectance and the link to surface wind speed. *Appl. Opt.* **1998**, *37*, 5550-5559.
28. Tratt, D.M.; Menzies, R.T.; Chiao, M.P.; Cutten, D.R.; Rothermel, J.; Hardesty, R.M.; Howell, J.N.; Durden, S.L. Airborne doppler lidar investigation of the wind-modulated sea-surface angular retroreflectance signature. *Appl. Opt.* **2002**, *41*, 6941-6949.
29. Cox, C.; Munk, W. Measurement of the roughness of the sea surface from photographs of the sun's glitter. *J. Opt. Soc. Amer.* **1954**, *44*, 838-850.
30. Bréon, F.M.; Henriot, N. Spaceborne observations of ocean glint reflectance and modeling of wave slope distributions. *J. Geophys. Res.* **2006**, *111*, doi:10.1029/2005JC003343.
31. Callaghan, A.H.; White, M. Automated processing of sea surface images for the determination of whitecap coverage. *J. Atmos. Oceanic Technol.* **2009**, *26*, 383-394.
32. Moore, K.D.; Voss, K.J.; Gordon, H.R. Spectral reflectance of whitecaps: Their contribution to water-leaving radiance. *J. Geophys. Res.* **2000**, *105*, 6493-6499.

33. Frouin, R.; Schwindling, M.; Deschamps, P.-Y. Spectral reflectance of sea foam in the visible and near-infrared: *In situ* measurements and remote sensing implications. *J. Geophys. Res.* **1996**, *101*, 14361-14371.
34. Kay, S.; Hedley, J.D.; Lavender, S. Sun glint correction of high and low spatial resolution images of aquatic scenes: A review of methods for visible and near-infrared wavelengths. *Remote Sens.* **2009**, *1*, 697-730.
35. Zarbock, H.W. Past, Present and Future Freshwater Inflow to Tampa Bay. Effects of a Changing Watershed. In *Proceedings of Tampa Bay Area Scientific Information Symposium 2*, St. Petersburg, FL, USA, 27 February–1 March 1991; pp. 23-24.
36. Lewis, R.R., III; Whitman, R.L., Jr. A New Geographic Description of the Boundaries and Subdivisions of Tampa Bay, In *Proceedings of Tampa Bay Area Scientific Information Symposium*, University of South Florida, Tampa, FL, USA, 3–6 May 1982; pp. 10-18.
37. Grabe, S.; Barron, J. Sediment contamination, by habitat, in the tampa bay estuarine system (1993–1999): Pahs, pesticides and pcbs. *Environ. Monit. Assess.* **2004**, *91*, 105-144.
38. Tyler, D.; Zawada, D.G.; Nayegandhi, A.; Brock, J.C.; Crane, M.P.; Yates, K.K.; Smith, K.E.L. *Topobathymetric Data for Tampa Bay, Florida*; US Geological Survey: Reston, VA, USA, 2007.
39. Ryan, W.B.F.; Carbotte, S.M.; Coplan, J.O.; O'Hara, S.; Melkonian, A.; Arko, R.; Weissel, R.A.; Ferrini, V.; Goodwillie, A.; Nitsche, F.; Bonczkowski, J.; Zemsky, R. Global multi-resolution topography synthesis. *Geochem. Geophys. Geosyst.* **2009**, *10*, Q03014.
40. Ross, S.M. Peirce's criterion for the elimination of suspect experimental data. *J. Eng. Technol.* **2003**, *20*, 38-41.
41. Moreno-Madrinan, M.J.; Al-Hamdan, M.Z.; Rickman, D.L.; Muller-Karger, F.E. Using the surface reflectance modis terra product to estimate turbidity in Tampa Bay, Florida. *Remote Sens.* **2010**, *2*, 2713-2728.
42. Wessel, P.; Smith, W.H.F. A global self-consistent, hierarchical, high-resolution shoreline database. *J. Geophys. Res.* **1996**, *101*, 8741-8743.